EUROFUSION WPPMI-PR(16) 15011

D Pfefferle et al.

Effects of magnetic ripple on 3D equilibrium and alpha particle confinement in the European DEMO

Preprint of Paper to be submitted for publication in
Nuclear Fusion

This work has been carried out within the framework of the EUROfusion Consortium and has received funding from the Euratom research and training programme 2014-2018 under grant agreement No 633053. The views and opinions expressed herein do not necessarily reflect those of the European Commission.

Effects of magnetic ripple on 3D equilibrium and alpha particle confinement in the European DEMO

D Pfefferlé[1*] , W A Cooper[1], A Fasoli[1], J P Graves[1]

[1] *École Polytechnique Fédérale de Lausanne (EPFL), Swiss Plasma Center (SPC), CH-1015 Lausanne, Switzerland*

Abstract

An assessment of alpha particle confinement is performed in the European DEMO reference design. 3D MHD equilibria with nested flux-surfaces and single magnetic axis are obtained with the `VMEC` free-boundary code, thereby including the plasma response to the magnetic ripple created by the finite number of TF coils. Populations of fusion alphas that are consistent with the equilibrium profiles are evolved until slowing-down with the `VENUS-LEVIS` orbit code in the guiding-centre approximation. Fast ion losses through the last-closed flux-surface are numerically evaluated with two ripple models: 1) using the 3D equilibrium and 2) algebraically adding the non-axisymmetric ripple perturbation to the 2D equilibrium. By virtue of the small ripple field and its non-resonant nature, both models quantitatively agree. Differences are however noted in the toroidal location of particles losses on the last-closed flux-surface, which in the first case is 3D and in the second not. Superbanana transport, i.e. ripple-well trapping and separatrix crossing, is expected to be the dominant loss mechanism, the strongest effect on alphas being between $100 - 200$ KeV. Above this, stochastic ripple diffusion is responsible for a rather weak loss rate, as the stochastisation threshold is observed numerically to be higher than analytic estimates. The level of ripple in the current 18 TF coil design of the European DEMO is not found to be detrimental to fusion alpha confinement.

* Present address: Princeton Plasma Physics Laboratory (PPPL), Princeton NJ, 08543-0451, USA

I. INTRODUCTION

A variety of physical and technological aspects must be taken into account while conceiving the prototype commercial fusion reactor DEMO. One important aspect in order to maintain optimal burning plasma conditions is the confinement of fusion alphas. Confinement primarily depends on the magnetic configuration, and can be evaluated in axisymmetry by neoclassical transport theory [1] and dedicated simulation tools, e.g. `TRANSP` [2]. Fast ion confinement is however significantly affected by the presence of non-axisymmetric magnetic fields; the non-conservation of toroidal momentum and large drift orbits lead to increased collisional and distinct collisionless loss channels. As a consequence, power deposition and heat loads can peak at specific toroidal locations [3–6], potentially damaging Plasma-Facing Components (PFCs).

Magnetic ripple due to the fixed finite number of Toroidal Field (TF) coils is a permanent source of toroidal asymmetry within tokamak plasmas. The amplitude of the ripple field is usually below 5% percent of the total field in existing tokamaks and predicted to be $< 2\%$ in ITER. It scales with the major radius raised to the power of the number of coils N [7, 8] and can be passively reduced by introducing Ferritic Inserts (FIs) between the TF coils [9]. Even with these features, magnetic ripple can have a sizeable impact on fast ion behaviour [10, 11]. At a collisionless level, the trapping of particles in toroidal magnetic wells can lead to superbanana transport [12, 13], and the onset of the stochastic motion of bounce tips [11, 14, 15] can occur, leading to fast vertical particle motion and early particle loss. Collisions ease particles in and out of ripple traps and regions of chaotic bounce tip motion, thus altering neoclassical transport regimes [16, 17]. In most studies, the ripple field is treated perturbatively, i.e. the non-axisymmetric components produced by the TF coils without the plasma is added to the axisymmetric equilibrium as a vacuum perturbation [18]. The approximations made on particle motion, such as zero orbit width expansions, are not necessarily valid throughout the broad energy spectrum of fast particle populations.

In this paper, an assessment of fusion alpha confinement in the European DEMO design is carried out. The main goal is to facilitate the calculation of alpha particle losses due to magnetic ripple in DEMO, and thus to be able to estimate power fluxes to the machine wall and plasma facing components in a realistic and consistent way. The first part of the effort is to establish of a suitable model for the plasma response to the breaking of

axisymmetry due to finite number of toroidal field coils. This particular study is motivated by the recent demonstration [19] that the plasma response model, employed to investigate the effect of axisymmetry breaking due to $N = 3$ resonant magnetic perturbation (RMP) coils, has a strong effect on fast ion confinement and the scaling of losses. In that study, and in this one, two opposing approaches are compared, one where the symmetry breaking field calculated in absence of the plasma is added to an axisymmetric MHD equilibrium calculation (henceforth called the *2D+ripple* approach), while the other where a full 3D free boundary MHD equilibrium calculation naturally includes the plasma response within the 3D deformation of its flux-surfaces (henceforth called the *3D equilibrium* approach). Confinement of fast particles in ITER has been similarly investigated with 3D equilibrium [20]. In the study into the effects of resonant magnetic perturbations on fast ion confinement [19], it was found that particle losses are dominated, at low energy, by parallel transport due to field-line stochasticity in the 2D+RMP approach and, at high energy, by cross-field drift in the 3D deformed equilibrium. The study reported here examines to what extent the two models of 3D fields lead to transport of alpha particles in DEMO where axisymmetry breaking is associated with the ripple of $N = 18$ TF coils. In this case, the plasma response in the presence of such high toroidal mode number is predicted to be weak, thus ensuring that field-line stochasticity is low and that both ripple models are equivalent representations of the physical situation.

The modelling comprises a realistic evaluation of the 3D vacuum fields produced by the DEMO coils using a Biot-Savart integrator `Coil.Sphell` [21], a consistent treatment of the plasma response as a 3D MHD equilibrium using the free-boundary `VMEC` code [22] and an accurate tracking of fast particles with the `VENUS-LEVIS` orbit code [23]. By undertaking full-F simulations for the alpha particle distribution function, it is found that the choice of ripple model affects the local power flux, i.e. the toroidal and poloidal deposition points on the LCFS, but the total power given to the edge is the same. Simulations predict an increase of 50% of the radiated power of $418kW$ through the LCFS in a purely axisymmetric system. Transport is found to be enhanced in the 100-200keV range, which constitutes a convenient process for helium ash removal dominated by collisional ripple trapping and superbanana transport, rather than stochastic ripple diffusion.

The paper is organised as follows. Section II describes the input parameters used for integrated modelling of DEMO, i.e. coil configuration and profiles. It also discusses the

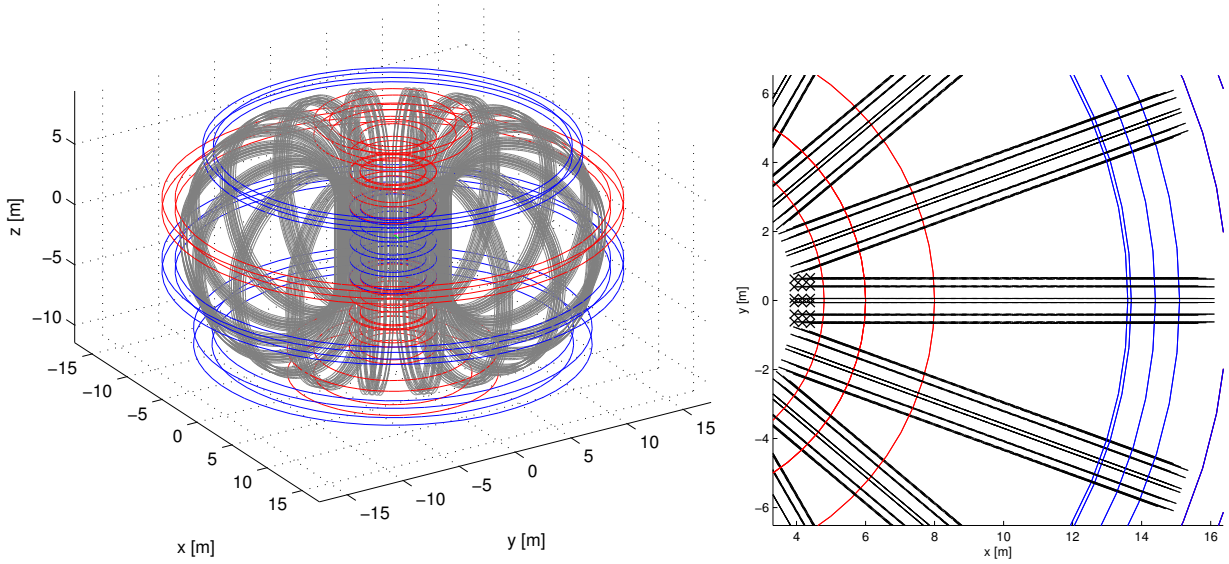

(a) 3D view of DEMO with 18 TF coils. Red/blue colours denote the direction of current (clockwise/counter-clockwise) in the PF coils.

(b) Top view of the TF coils. The crosses represent the discretised filaments on the midplane high-field side.

Figure 1: DEMO coils modelled as filaments for the computation of the 3D vacuum field (without plasma).

2D and 3D equilibria obtained with `VMEC` as well as the ripple field, represented either as a vacuum component or as the bulging of 3D nested flux-surfaces. Section III reviews the conditions for ripple-wells, superbanana orbits and stochastic ripple diffusion, which are important collisionless loss channels. Section IV presents the results from full-F slowing-down simulations within `VENUS-LEVIS` and gives an estimate of the alpha particle and power loss through the last-closed flux-surface (LCFS).

II. DEMO COILS, PROFILES, EQUILIBRIUM AND RIPPLE FIELD

A. Coils and vacuum fields

The European DEMO coil configuration consists of 18 TF coils (black curves), 6 control coils (blue squares) and a central stack of 5 coils (green rectangles), as depicted on figure 1 and 2. Each of the 18 TF coils are modelled with 18 evenly distributed current-carrying filaments, as highlighted by the crosses on figure 1(b). The curves formed by each of these

filaments are discretised into a large number of small straight segments. The control coils are modelled with 4 ring-shaped filaments on each corner and the stacked central coils either with 6 or 10 depending on their height. Figure 2 displays this setup in the poloidal plane; the magenta crosses or dots locate each filament and represent the direction of current (dots means outwards and crosses inwards with respect to the sheet of paper). The direction of current in the TF coils is such that the toroidal magnetic field points in the clockwise direction looking from above the device (opposite to the definition of cylindrical toroidal angle). In this way, the $\boldsymbol{\nabla} B$ drift is naturally downwards, towards the divertor. The induced toroidal plasma current is in the same direction as the magnetic field (flowing clockwise from above) as in ITER. This way, co-passing particles (with $v_{||} > 0$) have an inward radial drift on the upper half and outward drift on the lower half of their orbit.

`Coil.Sphell` [21] is used to process the vacuum field generated by the current filaments. Applying the Biot-Savart law, the code sums the contribution to the total field of each discretised segment [24, section 2.3d] as well as the Green functions (elliptic integral) of each axisymmetric PF filament weighted by the coil's current. The vacuum magnetic field B_R, B_Z, B_ϕ is recorded on a 3D cylindrical mesh in orthonormal cylindrical coordinates as an `mgrid` file that is then read by the free-boundary equilibrium code `VMEC` and the orbit solver `VENUS-LEVIS` [19]. The non-axisymmetric component of the vacuum field that gives rise to magnetic ripple is discussed in section II D.

B. Profiles

The background plasma profiles considered throughout this work have been established by the DEMO Physics Basis Group to model the Start Of Flat-top (SOF) phase of a generic pedestal H-mode discharge. A weakly reversed core q-profile and edge bootstrap current is assumed. The ion population consists of 50% Deuterium and 50% Tritium. Figure 3(a) displays the electron/ion densities/temperatures. The background plasma pressure is taken as the summed product $P = \sum_j n_j T_j$ and is used as an input for the force balance calculation within `VMEC` alongside the toroidal current density profile. These profiles as well as the q-profile resulting from the equilibrium calculation are shown on figure 3(b). The choice of q-profile is particularily important because ripple transport regimes are influenced by the field-line pitch, as pointed out by various authors [11, 25] and reviewed in section III. The

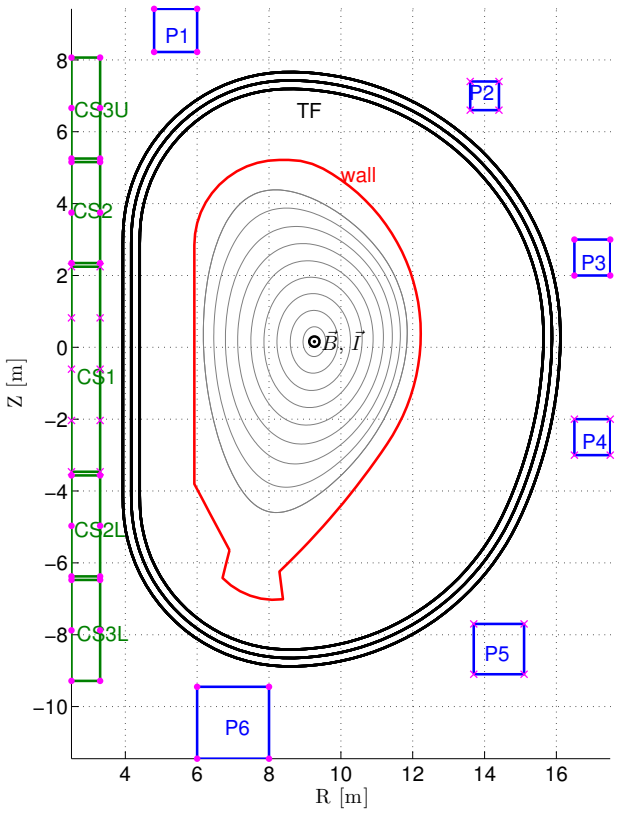

Figure 2: Poloidal cross section of DEMO coils, vessel wall (red contour) and 2D plasma flux-surfaces from `VMEC` calculation (grey curves). The black lines depict the filaments used to represent one TF coil. The TF coil current flows in the counter-clockwise direction, yielding a toroidal field coming out of the poloidal plane. The blue squares delimit the control PF coils and the green rectangles the central stack coils. The magenta marks represent the filaments chosen to model the PF coils (crosses for inward current direction, dots for outward).

current profile and the pressure profile have a direct influence on the equilibrium calculation via the MHD force-balance. The temperature and density profile control the fusion cross-section and therefore the source of alpha particles in full-F simulations. It is rather tedious to perform a sensitivity study of alpha particle losses with respect to background plasma profiles. The latter are still under investigation and have not acquired their definite shape, such that it is probably too early to perform quantitative scans. The numerical results presented hereafter suggest that alpha particle confinement is excellent in DEMO and loss due to ripple is a minor concern. Thanks to the tools and work presented here, losses can easily be re-assessed based on analytic expressions reviewed in section III.

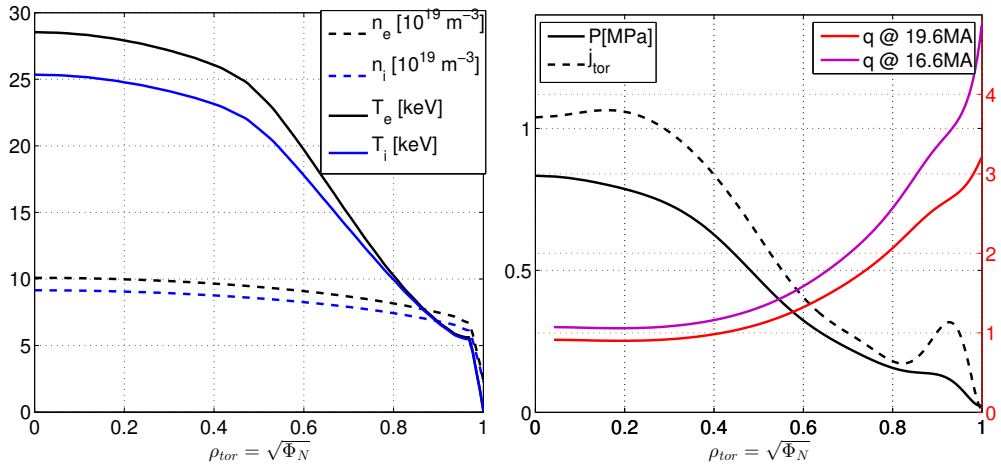

(a) Generic density and temperature profiles, used as input for `VMEC` free-boundary calculations.

(b) Pressure and toroidal current density (inputs for `VMEC`) as well as q-profile (output of `VMEC`).

Figure 3: DEMO background profiles at the SOF phase.

C. Equilibrium

The details of the construction of free boundary equilibrium using the `VMEC` code is presented in detail in [26]. Given the external vacuum field from the coils described in section II A and the profiles described in section II B, non-linear MHD equilibrium calculations are performed with the free-boundary `VMEC` code. Two kinds of magnetic configurations are produced: an axisymmetric equilibrium with toroidal mode number $n = 0$ and a 3D equilibrium with multiples of the toroidal ripple periodicity $n = \pm\{0, 1, 2, 3\} \times N$, where $N = 18$ is the number of TF coils. In both cases, fully up-down asymmetric mode content and poloidal numbers $m = 0{-}11$ are retained. The number of radial mesh points is set to 289. The 2D equilibrium obtained represents the unperturbed axisymmetric plasma to which the vacuum ripple field is algebraically added. The 3D equilibrium includes the plasma response to the magnetic ripple in the geometry of its nested flux-surfaces as well as in the toroidal mode spectrum of the magnetic field. In this sense, the `VMEC` MHD equilibria are consistent with the profiles and coil setup presented earlier. The studied DEMO configuration is a single-null diverted plasma with major radius $R_0 = 9.25$m, minor radius $a = 2.9$m, field on-axis $B_0 = 6$T, toroidal plasma current $I_p = 19.6$MA, volume $V = 2145m^3$ and $\beta = 2.2\%$. Figure II C illustrates the corrugation of the LCFS due to the finite number of TF coils in

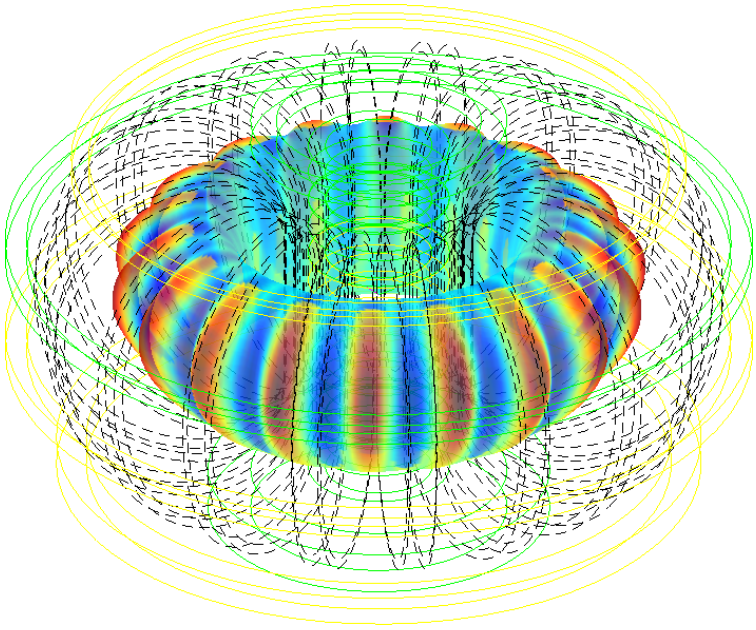

Figure 4: Representation of the bumpy LCFS of a 3D MHD equilibrium computed by the free-boundary `VMEC` code in the DEMO coil configuration. The corrugation caused by the ripple, $\boldsymbol{R}_{3D} - \boldsymbol{R}_{2D}$, has been inflated by a factor of 200 for illustration purposes. Deformations of the LCFS are found to be 1cm at most.

coil	MA	coil	MA
TF	14.832	P1	12.28
CS3U	9	P2	-7.2 / -6.8
CS2	5.6	P3	1.25 / 1.65
CS1	-8.79	P4	-8.58 / -8.18
CS2L	7.01	P5	-7.11 / -6.71
CS3L	8.7	P6	18.3 / 18.3

Table I: Coil current required to centre and stretch the plasma in the limits of the vacuum vessel with `VMEC` for DEMO $I_p = 19.6$MA / 16.6MA.

the 3D equilibrium. The maximum edge deformation is found not to exceed 1cm, suggesting that the non-linear response of the plasma is weak. The coil currents required to centre and stretch the plasma in place are shown in table I. It is noted that the plasma position and the shape of the LCFS are rather sensitive to small changes in these values. An MHD stability analysis would help understand the nature of this sensitivity.

D. Ripple field

The non-axisymmetric component of the magnetic field, i.e. the ripple $\delta\boldsymbol{B}$, is represented in the literature as a vacuum field. With this simplifying assumption, the perturbation respects $\boldsymbol{\nabla}\cdot\delta\boldsymbol{B}=0$ and $\boldsymbol{\nabla}\times\delta\boldsymbol{B}=0$. The plasma response to a weak non-resonant term is important if $\beta\gtrsim N^2\epsilon^2$, where $\epsilon=r/R$ is the inverse aspect ratio [8, Newcomb's equation in a cylindrical plasma column]. It is unlikely that this condition be satisfied in the case of DEMO. This statement is yet to be verified numerically by comparing the ripple amplitude in the 2D+ripple and 3D equilibrium models.

In the vacuum approximation, the ripple field satisfies a Laplace equation $\boldsymbol{\nabla}^2\Phi=0$, where $\delta\boldsymbol{B}=\boldsymbol{\nabla}\Phi$. Analytic solutions of this boundary value problem exist in special cases. For circular TF coils in a tokamak configuration, the fundamental ($n=N$) vacuum ripple perturbation is expressed as [7]

$$\Phi=\frac{B_0R_0}{N}\delta(R,Z)\sin(N\phi) \tag{1}$$

$$\delta(R,Z)=\delta_0\cosh(\alpha Z)J_N(\alpha R) \tag{2}$$

where J_N is the Bessel function of order N and α and δ_0 are geometric constants. This result highlights the fact that the ripple amplitude scales as $\delta\propto(\alpha R)^N$ as a function of major radius and number of TF coils. The geometry is more complicated than circular in DEMO, so the ripple amplitude $\delta(R,Z)$ is evaluated numerically as

$$\delta(R,Z)\equiv\frac{B_{\phi,max}-B_{\phi,min}}{B_{\phi,max}+B_{\phi,min}}=\frac{\max(B_\phi)}{<B_\phi>}-1 \tag{3}$$

where the total 3D field $\boldsymbol{B}$ is calculated via `Coil.Sphell` or `VMEC`. The fundamental field and vector potential (up to a choice of gauge) are then described by

$$\delta\boldsymbol{A}=\frac{B_0R_0}{N^2}R\cos(N\phi)\left(\partial_Z\delta\boldsymbol{\nabla}R-\partial_R\delta\boldsymbol{\nabla}Z\right) \tag{4}$$

$$\delta\boldsymbol{B}=B_0R_0\left[\tfrac{1}{N}\sin(N\phi)\boldsymbol{\nabla}\delta+\delta\cos(N\phi)\boldsymbol{\nabla}\phi\right]. \tag{5}$$

Figure 5(a) shows the non-axisymmetric component of the vacuum field generated by the coils as a function of the toroidal angle at a given point in (R,Z). The ripple field displays the expected sinusoidal behaviour with a dominant mode number $n=N$, as in equation (1). The magnetostatic interaction with ferritic inserts will reduce the amplitude of that

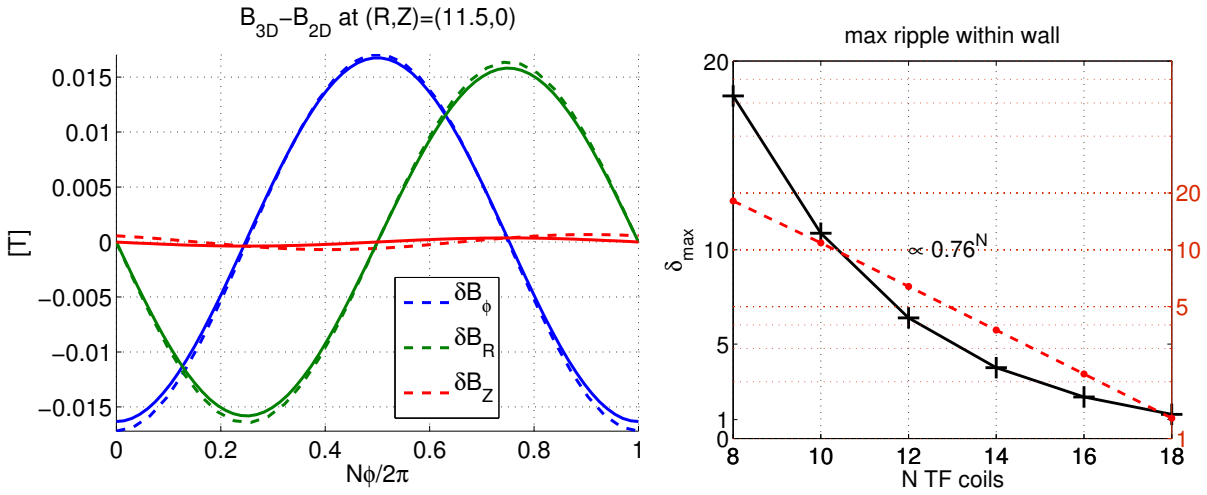

(a) Non-axisymmetric components of the vacuum field (ripple field) at the outer midplane at $R = 11.5$m within a field periodicity. Solid lines are vacuum fields from `Coil.Sphell` and dashed lines are from 3D equilibrium calculation with `VMEC`.

(b) Scaling of the maximum ripple within the vacuum vessel with respect to number of TF coils. The black curve refers to the linear axis (left) and the red curve to the logarithmic axis (right).

Figure 5: Properties of the ripple field of DEMO.

fundamental mode, but may give rise to harmonics and localised peaks [27]. Tools exist to model this phenomenon, but its investigation is outside the scope of this work.

Figure 5(b) demonstrates a scaling of $\delta_{max} = 0.76^N$ of the maximum ripple amplitude within the vacuum vessel as a function of the number of TF coils. The ripple amplitude in the current DEMO design is 0.72% with 18 coils. Keeping the vacuum vessel in place, it would be 1.24% with 16 and reduced to 0.41% with 20. The change is probably not significant enough to consider varying the number of coils. This is discussed from the point of view of alpha particle loss channels in section III.

Figure 6 shows that $\delta(R, Z)$ has the same features in the poloidal plane as in equation (2). It also demonstrates that the vacuum vessel is adequately positioned away from the large increase near the TF coils. Lowering the vacuum chamber by a few centimetres might help to further reduce its penetration.

Resonant magnetic perturbations generate magnetic islands at rational surfaces when applied to axisymmetric MHD equilibria and spoil the confining properties of nested flux-surfaces. When islands overlap, field-lines become stochastic, large portions of the plasma

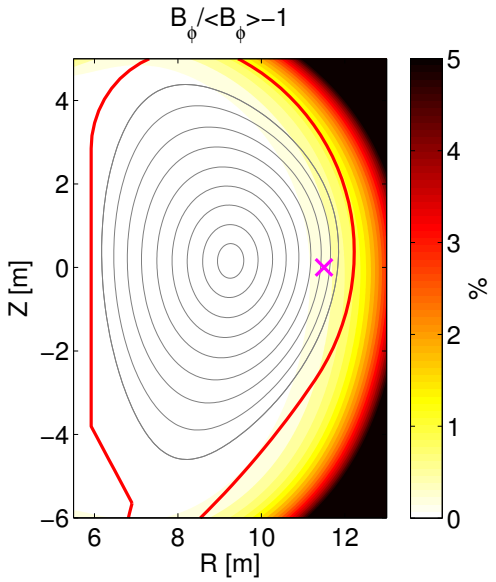

Figure 6: Poloidal cross-section of the relative ripple field amplitude. The magenta cross is where the components are evaluated in figure 5(a).

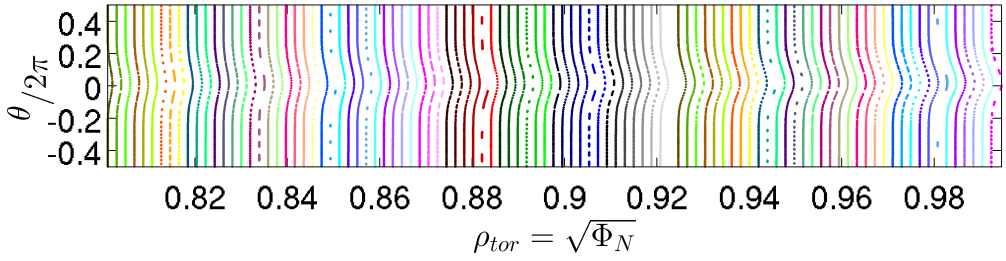

Figure 7: Poincaré plot of field-lines from the 2D+ripple model in the normalised flux coordinates plane (ρ_{tor}, θ). The nested flux-surfaces are weakly bulging out at the outer midplane. Displacements are in the range of 1cm in real space, similarly to figure II C.

are connected and relax to Taylor states [28]. In such cases, neither the 2D+ripple nor 3D equilibrium approach is appropriate to describe the magnetic configuration. Figure 7, which is a Poincaré plot of DEMO's field-lines, indicates that the ripple field is only weakly resonant and small enough not to destroy the nested flux-surfaces; the vertical lines are merely deformed and no islands form. Unlike the case of RMPs [19], both 2D+ripple and 3D equilibrium models are almost equivalent representations of the magnetic field.

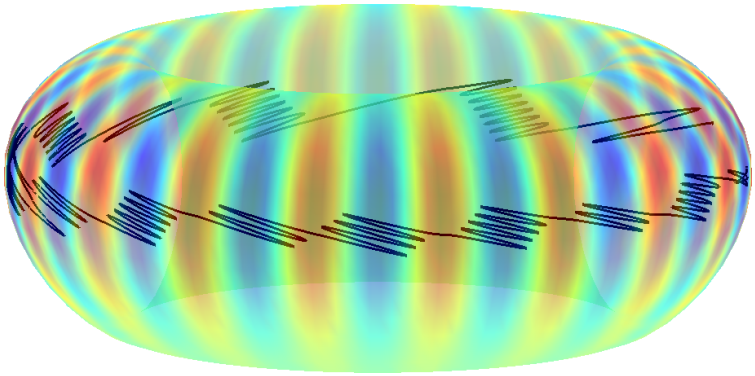

Figure 8: Trajectory of a deeply trapped particle shown on a torus with colour coding marking the ripple field intensity $|\delta B|$ on the average flux-surface. The particle is toroidally trapped until the downward $\boldsymbol{\nabla} B$ drift drags it away from the locally high ripple field so that the particle crosses to the next field periodicity. This mechanism, called separatrix-crossing [12, 13] leads to enhanced transport in the presence of collisions [7, 17].

III. ALPHA PARTICLE LOSS CHANNELS

In its minimum field of 4.6T, alpha particles at 3.5MeV in DEMO have a Larmor radius of 8.15cm at most, i.e. less than 3% of the minor radius (2.9m). With a poloidal field of 1.2T at the LCFS on the low-field side midplane, the banana width is expected to be $r_b = 2\sqrt{\epsilon} mv/eB_p \approx 30$cm, implying that first orbit loss concern alpha particles only in the outer 19% of the plasma volume. Additional losses will occur if particles access that space via collisionless and/or collisional processes. There is a distinction to make depending on whether the loss channel is effectively diffusive or convective. The diffusive type can be understood as the result of a "slow" stochastic processes (random walk), e.g. collisions or ergodic orbits. Losses from convection, which are in a sense direct and fast, are important to assess by solving the particle dynamics.

In the absence of collisions, the first-order guiding-centre drift equations admit three constants of motion in axisymmetric systems, namely energy $E = \frac{1}{2}mv^2 = \frac{1}{2}mv_{||}^2 + \mu B$, magnetic moment $\mu = mv_{\perp}^2/2B$ and toroidal momentum $P_\phi = eA_\phi + mv_{||}B_\phi/B = -e\Psi_p + mv_{||}F/B$ where Ψ_p is the poloidal flux and $F(\Psi_p) = B_\phi$ is the poloidal current and covariant component of the magnetic field. In axisymmetry, guiding-centre orbits are thus exactly integrable, i.e. can be expressed as quadratures. Magnetic ripple only spoils the conservation of toroidal momentum. Depending on the size of the perturbation, orbits change from being

near-integrable (deformed closed paths in phase-space) to resonant (island structures in phase-space) to finally chaotic/stochastic. Only when the orbits are stochastic/ergodic can collisionless losses effectively be described as a diffusion, otherwise they are convective in nature. The transition between topological classes of orbits is a difficult non-linear problem where the geometry, up-down asymmetry, elongation and triangularity have strong effects, as discussed hereafter.

In DEMO, the free orbits of passing particles do not deviate significantly enough from integrability, since the ripple is non-resonant and weak; the trajectories of passing particles form drift-surfaces that are topologically the same as flux-surfaces, traced by field-lines. Passing-particles are well confined and their contribution to heat loss and power deposition is negligible. Trapped particles, on the other hand, are extensively affected by non-axisymmetric components. Two different mechanisms are at play: 1) the perturbed position of their bounce-tips on a given $|B| = \text{const}$ surface can resonate with the ripple periodicity and become chaotic, leading to collisionless stochastic diffusion [15], 2) the toroidal variation of the ripple field creates magnetic mirrors such that particles with $v_{||}/v < \sqrt{\delta}$ become trapped within a field periodicity [7, 25]. In this case, the bounce tips rapidly move across the constant $|B|$ surface due to the "grad-B" drift in the $\boldsymbol{B} \times \boldsymbol{\nabla} B$ direction (downwards in our case), forming the so-called superbanana orbits. If the depth of the ripple well increases as the bounce tips are displaced outwards, the particle is lost to the edge. In the opposite case, the particle simply moves out of the ripple well and the orbit returns to being a traditional banana (poloidally trapped). The latter possibility, called ripple-detrapping or separatrix crossing [12, 13] is illustrated on figure 8. Such particles are still confined but traverse between periodicities in an random way.

A. Estimate of the ripple well domain

Regions where ripple wells exist are mapped at zero-order in Larmor radius by locating where the modulus of the total field,

$$B = B_{2D} + \delta B_{||} + O(\delta^2) = B_{2D}[1 + \delta \cos(N\phi)] + O(\delta^2), \tag{6}$$

has a negative slope (dip) in the direction of unperturbed field-lines [7, 25]. Writing the field-line equation $d\phi/d\theta = B^{\phi}_{2D}/B^{\theta}_{2D} \approx q$, where $B^i = \boldsymbol{B} \cdot \boldsymbol{\nabla} u^i$ are the contravariant components

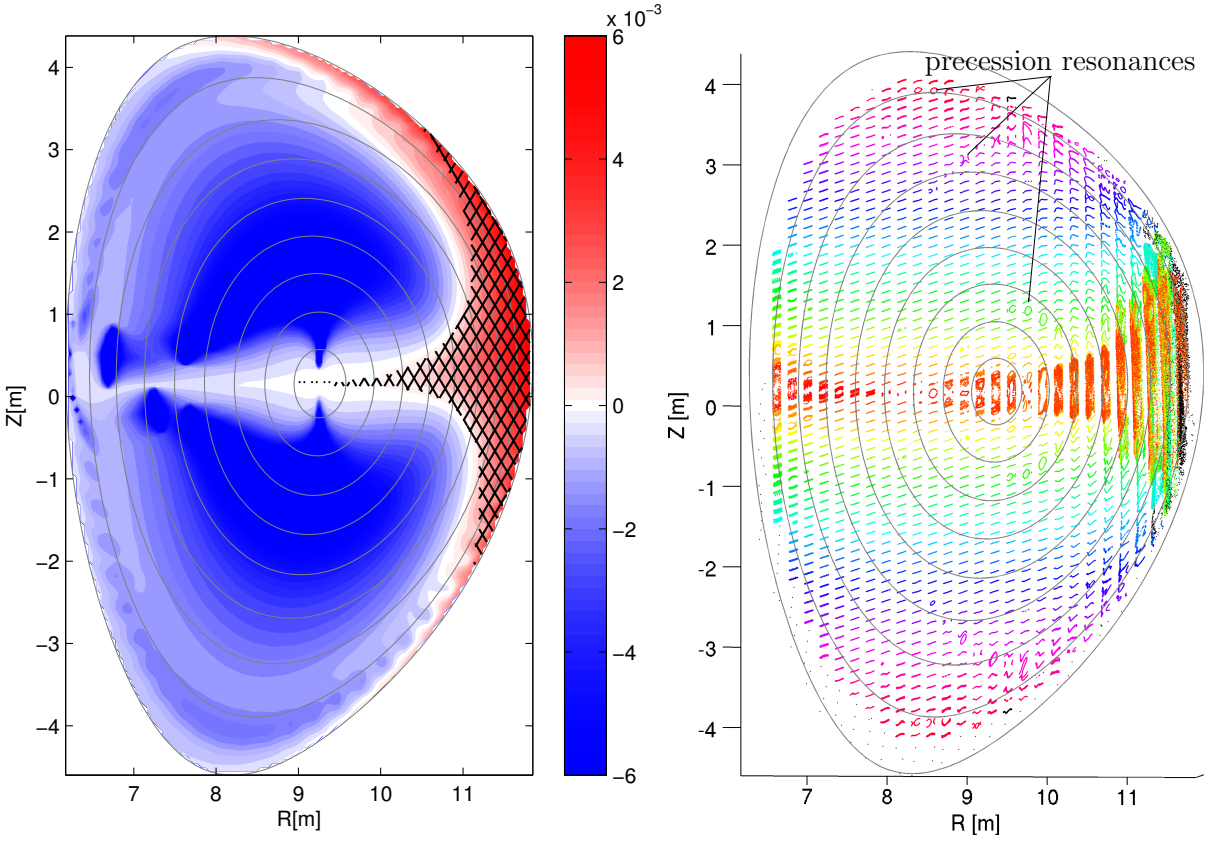

(a) The black hatched triangular region represents the ripple-well domain within the LCFS according to equation (7). The red region is where the ripple amplitude is larger than the threshold for stochastic ripple diffusion, i.e. $\delta - \delta_{GWB} \gtrsim 0$ (see equation (17)). Blue is where this difference is negative. If these regions span vertically to the LCFS, a path exists for particles to become lost.

(b) Displacement of 3.5MeV alpha particle bounce-tips due to the ripple field in the 2D+vacuum model simulated with guiding-centre orbit code `VENUS-LEVIS`. Each dot is a bounce-tip and each colour denotes a different particle. The outer midplane is where the ripple-well domain and the region for stochastic ripple diffusion overlap and the bounce tips are most affected. The picture is similar for the 3D equilibrium model.

Figure 9: Comparison between a) semi-analytical estimates of ripple-well and stochastic ripple diffusion domains and b) numerical integration of particle orbits.

of the magnetic field, the criterion is $0 > \frac{dB}{dl} = \frac{d\theta}{dl}\left(\partial_\theta B + q\partial_\phi B\right)$. Ripple wells occur roughly

when

$$\delta > \frac{|\partial_\theta B_{2D}|}{B_{2D} N} \frac{B^\theta_{2D}}{B^\phi_{2D}} \approx \frac{\epsilon |\sin\theta_b|}{Nq} \tag{7}$$

where $\epsilon = r/R$ is the inverse aspect ratio, $B_{2D} \approx B_0(1 - \epsilon\cos\theta)$, B_0 is the magnetic strength on axis. The fields in equation (7) are evaluated at the bounce position θ_b where the parallel velocity is zero, $v_{||} = 0$, and the guiding-centre energy is entirely stored in the magnetic potential, i.e. $E = \mu B_{2D}(\Psi_p, \theta_b)$. Notice that the first part of equation (7) is valid in any flux coordinate system, which makes it directly applicable to the output of `VMEC` (no need to find straight field-line coordinates).

The black hatched patch in figure 9(a) highlights the ripple well domain using equation (7) within the 19.6MA DEMO equilibrium. A direct vertical path to the LCFS appears beyond $R = 11$m from the outer midplane; particles whose bounce-tips fall into that area are rapidly lost (convection). Below $R = 11$m, trapped particles in the hatched domain move in and out of the ripple-well, as in figure 8. In velocity space, it is known that ripple-well trapping concerns only a small fraction $v_{||}/v \lesssim \sqrt{\delta}$ of the fast particle population [7, 29]. This loss channel is very active in the collisional regime, when particle orbits considerably vary due to pitch-angle scattering. The superbanana fraction is greatly enhanced by diffusion and redistribution of particles in phase-space [7, 13, 17].

B. Resonant bounce-tip motion and stochastic ripple diffusion

Figure 9(b) shows the bounce tip displacement of a collection of trapped particles. Their motion is numerically calculated by using the guiding-centre orbit code `VENUS-LEVIS`. Particles that are not ripple-trapped, which is the case for most of the dots in figure 9(b), can still become unconfined via a collisionless process called stochastic ripple diffusion [11, 14–16, 30]. Figure 10, which is a break-up of figure 9(b) into planes of constant major radius R, illustrates various examples of bounce-tip motion. Most appear to be only weakly perturbed (still integrable orbits) and form horizontal lines in the vertical and toroidal plane at constant B (KAM surfaces in phase-space). In some areas, the net toroidal shift matches the ripple field periodicity and the bounce-tip displacement resonates with the perturbation (in the sense of the KAM theorem), thus generating island structures and fixed points. The elliptic shapes at $R = 9.8$m and $Z = 1$m are examples of precession resonance, also indicated on figure 9(b). These resonant island structures grow and deform due to non-linearities, as

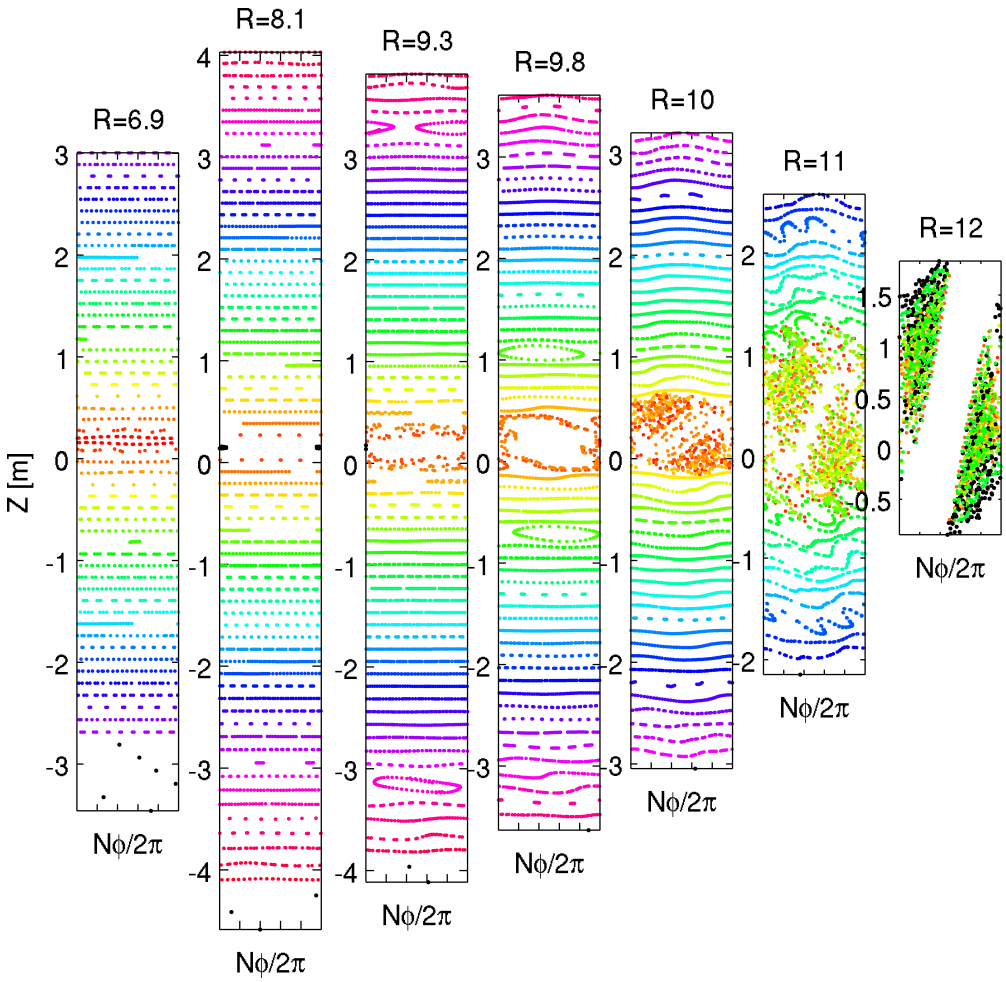

Figure 10: Displacement of bounce tips on different planes of constant $|B|$.

the ripple field becomes larger towards the outboard side (for example at $R = 11$m above $Z = 1.2$m). Eventually, the islands overlap and the wandering of the bounce-tips becomes chaotic, as seen near the midplane at $R = 11$m. This stochastic motion leads to collisionless diffusion and, if these regions connect to the vacuum vessel, particles are lost after several bounce times (~ 1000). The route to chaos is a highly non-linear problem [15] and the competition between *bounce resonances* and *precession resonances* leads to subtle changes in the resonance patterns.

There is no simple analytic expression for the onset of bounce-tip stochastisation and no reliable expression to trace out loss paths. Estimates are provided in the form of a Chirikov criterion applied to the bounce-tip map. Analytic expressions are established in the limit of zero orbit width by several authors [11, 14, 29]. Their result is generalised here to be able to directly use `VMEC` equilibria and coordinates. For a given energy E and magnetic

moment μ, the variables required to locate the bounce tips of a particle is the toroidal angle ϕ and toroidal momentum $-P_\phi/e = J$. The poloidal bounce point at $\Psi_p(E, \mu, J, \phi)$ and $\theta_b(E, \mu, J, \phi)$ is constrained by the relation $B(\Psi_p, \theta_b, \phi) = E/\mu$. In the absence of ripple, ϕ is an ignorable angle and J is the associated constant action, which conveniently corresponds to the poloidal flux $J = \Psi_p$. Following the work by [14], the weak ripple makes J become a time-dependent function, described by

$$\frac{dJ}{dt} = \frac{\partial \mathcal{L}/e}{\partial \phi} = v_{||}(\partial_\phi A_i) b^i_{2D} - \tfrac{\mu}{e}\partial_\phi B + O(\delta^2, \tfrac{m}{e}) \tag{8}$$

$$\approx \delta \tfrac{\mu}{e} B_{2D} N \sin[N\phi(t)] + O\left(\delta^2, \tfrac{m}{e}\right) \tag{9}$$

where equation (6) was used as well as the phase-space guiding-centre Lagrangian [31], $\mathcal{L} = (e\boldsymbol{A} + m v_{||}\boldsymbol{b})\cdot\dot{\boldsymbol{X}} - \frac{1}{2}m v_{||}^2 - \mu B$, $b^i = \boldsymbol{B}/B\cdot\boldsymbol{\nabla}u^i$ and the lowest-order unperturbed solution to the guiding-centre Euler-Lagrange equations $\dot{\boldsymbol{X}} = v_{||}\boldsymbol{b} + O(\frac{m}{e})$. By virtue of equation (4), the first term in equation (8) is equal to $v_{||}B_0R_0R/N[(\boldsymbol{b}\times\hat{\boldsymbol{e}}_\phi)\cdot\boldsymbol{\nabla}\delta)]\sin(N\phi) \propto \dot{\phi}\sin(N\phi)$ and contributes little to the total variation. As in [14], the stationary phase approximation is used to integrate equation (9) around the bounce tip, $-P_\phi/e = J$ is incremented at the j^{th} bounce tip by

$$J_{j+\frac{1}{2}} = J_{j-\frac{1}{2}} + \Delta \sin\left[N\phi_j + (-1)^j \pi/4\right] \tag{10}$$

$$\text{where} \quad \Delta(E, \mu, J) = \delta \frac{\mu}{e} B_{2D} \sqrt{\frac{2\pi N}{|\ddot{\phi}_j|}} + O(\delta^2, \tfrac{m}{e}) \tag{11}$$

The fields in this expression are evaluated at the bounce position in the unperturbed equilibrium. The subscript $B_{2D} = B$ is dropped hereafter so as not to overload the notation. The toroidal acceleration is found at lowest order in the drift approximation as

$$\ddot{\phi} \approx \frac{d}{dt}\left[v_{||}\frac{B^\phi}{B}\right] \approx \dot{v}_{||}\frac{B^\phi}{B} = -\frac{e}{m}\frac{\mu}{e}\frac{\partial_\theta B}{B}\frac{(B^\phi)^2}{qB} \tag{12}$$

where the equation of motion $\dot{v_{||}} = -\frac{e}{m}\frac{\mu}{e}\boldsymbol{\nabla}B\cdot\boldsymbol{b}$ was used. The coefficient Δ, which represents the displacement in J of the bounce tip at each bounce, is thus approximately

$$\Delta = \delta \frac{B}{B^\phi}\sqrt{\frac{\pi N q}{\partial_\theta B/B}\frac{2m\bar{E}}{e}} \tag{13}$$

where $e\bar{E} = \mu B = 3.5\text{MeV}$ and $B^\phi = \boldsymbol{B}\cdot\boldsymbol{\nabla}\phi = F/R^2$ the contravariant toroidal component of the magnetic field in an axisymmetric tokamak. The modulus of $B \approx F/R$, so that the

fraction is approximately $B/B^{\phi} \approx R$. The reader may verify that Δ has the right units of flux, i.e. $[\mathrm{kg}m^2/Cs]$. It is noted that this result differs from [15, equation (5)].

Between tips j and $j+1$ (lower and upper or vice-versa), the toroidal angle jumps by

$$\phi_{j+1} = \phi_j - (-1)^j \phi_{b,j+\frac{1}{2}} + \phi_{p,j+\frac{1}{2}} \tag{14}$$

where $\phi_b(E,\mu,J) = 2q\theta_b(E,\mu,J)$ is the toroidal angle after travelling along the field-line from $-\theta_b$ to θ_b (assuming up-down symmetry) and $\phi_p(E,\mu,J)$ is the displacement due to precession drift. Equations (10) and (14) describe a discrete map. There is a myriad of periodic points for which $\Psi_{j+K} = \Psi_j$ and $N\phi_{j+K} = N\phi_j + 2k\pi$. Island structures can form around them, as the map resonates with the perturbation. The width of these islands is obtained by expanding linearly around the periodic points. According to Chirikov, stochastic behaviour is triggered when this width surpasses the distance to the neighbouring periodic point. Following [11, 15], the island width scales as $w_K \approx \sqrt{4\Delta/N(|\phi_b'| + |\phi_p'|)}$ and the separation as $\Psi_{K+1} - \Psi_K \approx 2\pi/N(|\phi_b'| + |\phi_p'|)$, where prime denotes derivative with respect to J (at fixed energy and magnetic moment). The variation of ϕ_b is expressed as

$$\phi_b' = 2q'\theta_b + 2q\theta_b' \tag{15}$$

where the bounce angle is constrained to vary as

$$dB(\Psi_p, \theta_b) = 0 \iff \frac{d\theta_b}{dJ} = -\frac{\partial_{\Psi_p} B}{\partial_\theta B} \tag{16}$$

The variation of precession angle ϕ_p' cannot be expressed in terms of simple analytic expressions. It is often the case that $|\phi_p'| \ll |\phi_b'|$ in tokamaks so that ϕ_p' can be neglected. The Chirikov criterion then reads $w_K^2/(\Psi_{K+1} - \Psi_K)^2 \approx N\Delta|\phi_b'| \gtrsim 1$ and the stochastic ripple diffusion is found (within an order of magnitude) to occur wherever $\delta \gtrsim \delta_{GWB}$, with

$$\delta_{GWB} \equiv \frac{B^{\phi}}{B}\sqrt{\frac{e}{2m\bar{E}}\frac{\partial_\theta B/B}{\pi N^3 q}}\left|2q'\theta_b - 2q\frac{\partial_{\Psi_p} B}{\partial_\theta B}\right|^{-1} = \frac{\psi_e F}{R^2 B}\sqrt{\frac{e}{2m\bar{E}}\frac{\partial_\theta B/B}{\pi N^3 q^3}}\left|2\frac{dq}{ds}\theta_b - 2q\frac{\partial_s B}{\partial_\theta B}\right|^{-1} \tag{17}$$

where $s = \psi_t/\psi_e$ is the normalised toroidal magnetic flux, a more natural radial coordinate used by `VMEC`. Its relation with the poloidal flux is straight-forward, as $d\psi_t/d\Psi_p = q$. The reader can verify that equation (17) reduces correctly to the expression by [11] for a large aspect ratio circular flux-surface expansion of tokamak geometry (evaluated at $\theta_b = \pi/2$)

$$\delta_{GWB} \approx \left(\rho\frac{dq}{dr}\right)^{-1}\left(\frac{\epsilon}{\pi N q}\right)^{3/2} \tag{18}$$

where $\rho = mv_\perp/eB = \sqrt{2\frac{m}{e}\bar{E}}/B$ is the Larmor radius, $r = a\sqrt{s}$ and a the minor radius. This expression is useful to understand the scaling of the threshold for stochastic ripple diffusion in terms of basic equilibrium parameters. Larger values of q and higher magnetic shear reduce the threshold, consequently spoiling the confinement of trapped bananas. In a diverted plasma where $q \to \infty$ at the separatrix, stochastisation of the bounce motion will always occur beyond a given radius. What matters is whether there a direct path to the wall exists and how many alpha particles are found in those domains.

Equation (17) is applied to predict the regions of chaotic bounce tip motion in figure 9(a). The red patch near the outer edge shows where the threshold for stochastisation ripple diffusion is exceeded. It qualitatively matches the region where bounce tips are observed to be strongly affected by the ripple in figure 10. The blue colour represents the areas where $\delta - \delta_{GWB}$ is negative and the orbits are near-integrable (no overlap of islands). The accuracy of this criterion is poor for such small ripple amplitude. Equation (17) tends to over predicts the level of stochastic bounce orbits in the case of DEMO. The numerical integration of particle motion such as in figure 10 indicates that alpha particles are actually better confined than is predicted by the analytic estimate. Applying equation (18) leads to a worse mismatch. The criterion for the onset of stochastic ripple diffusion could be further improved by including ϕ'_p, finite orbit width effects, higher-order terms in δ, etc... However, with the availability of particle pushing codes, it is more reliable to obtain the threshold by solving particle orbits directly.

An interesting point to mention in figure 10 is that the resonant/chaotic structures are vertically separated by straight lines. The ripple setup of DEMO appears to be favourable to the existence of robust KAM barriers. Assessing their stability can actually serve as a proxy for design optimisation. In this work, the regions of stochastic ripple diffusion and ripple wells have been mapped inside the plasma, where alpha particles are expected to be created. Extending the study to beyond the LCFS is not possible with `VMEC` under the assumption of nested flux-surfaces.

IV. RESULTS FROM SLOWING DOWN SIMULATIONS

The previous section has demonstrated that it is possible to estimate the collisionless loss channels, but only in simple geometries and under many assumptions. Full-F PIC simula-

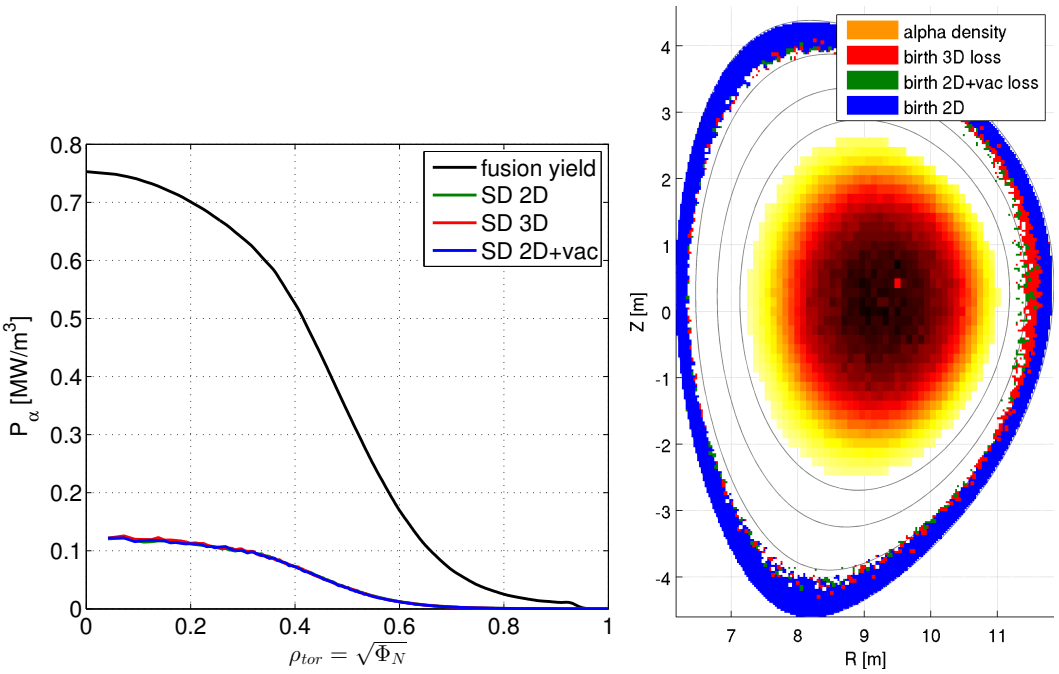

(a) Top curve is the alpha power density from fusion cross-sections and the selected background profiles (dependent on temperature and density) and saturated distribution. Bottom curves are saturated alpha particle power densities from slowing-down simulations in various ripple models.

(b) Saturated alpha population density versus birth region of lost particles.

Figure 11: Fusion yield (initial source of alpha particles), saturated power and birth regions of lost particles.

tions with `VENUS-LEVIS` are required to model the effect of collisions and yield quantitative estimate of alpha particle losses. First, a list of markers is created according to the fusion cross section between thermal Deuterium and Tritium [33]. Figure 11(a) displays the alpha power density calculated using the background profiles of section II B. A fixed number of markers are injected at regular time intervals and their orbits are followed until they either reach thermal energy via slowing-down processes (thermalisation) or cross outside of the LCFS because of prompt loss, pitch-angle scattering and the convective/diffusive processes associated to ripple, as described in section III. Collisions against the background plasma (electrons and ions) are modelled via Monte-Carlo operators [32]. After a period corresponding to a slowing-down time, the alpha particle distribution saturates and the loss fluxes are

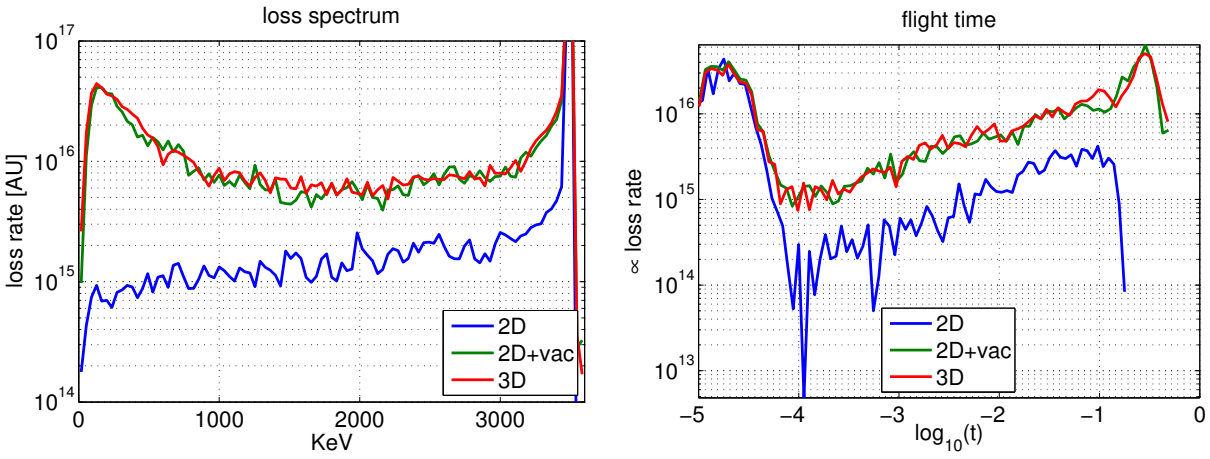

(a) Energy spectrum of losses.

(b) Flight time of lost particles.

Figure 12: Histograms of losses across the LCFS for axisymmetric case, 2D+ripple and 3D equilibrium ripple models.

compared for different equilibria and ripple models.

The lower curves on figure 11(a) show the saturated alpha particle power remaining in the hot distribution - most markers have transferred their energy to the bulk plasma and left the distribution or have hit the LCFS. The difference between the axisymmetric equilibrium and the cases with ripple is imperceptible in the scale of the figure. Indeed, given the background temperature and density profiles, the alpha birth position is strongly centred in the core, where particles are well confined. This is depicted on figure 11(b), which compares the central region of high fusion yield (orange heat map) with the zones where lost particles were initially emitted. The total power radiated through the LCFS obtained from the simulations is 418kW assuming a purely axisymmetric equilibrium, 674kW in the 2D+ripple model and 662kW for the 3D equilibrium case. Comparing to a total fusion power of 450MW, a low level of alpha power is expected to be lost. The finite number of toroidal field coils (18 field coils) effectively increases the level by fifty percent.

Figure 12(a) shows a histogram of lost particles as a function of their energy at the LCFS. The peak at 3.5MeV corresponds to prompt losses, accounting for most of the lost alpha power. The curve then decreases in the axisymmetric equilibrium, as particles lose energy and become better confined, and rises again at around $100 - 200$KeV in both 2D+ripple and 3D equilibrium models. This is a consequence of ripple enhanced collisional transport [7, 17]. The increase of transport at low energy is convenient for helium ash removal.

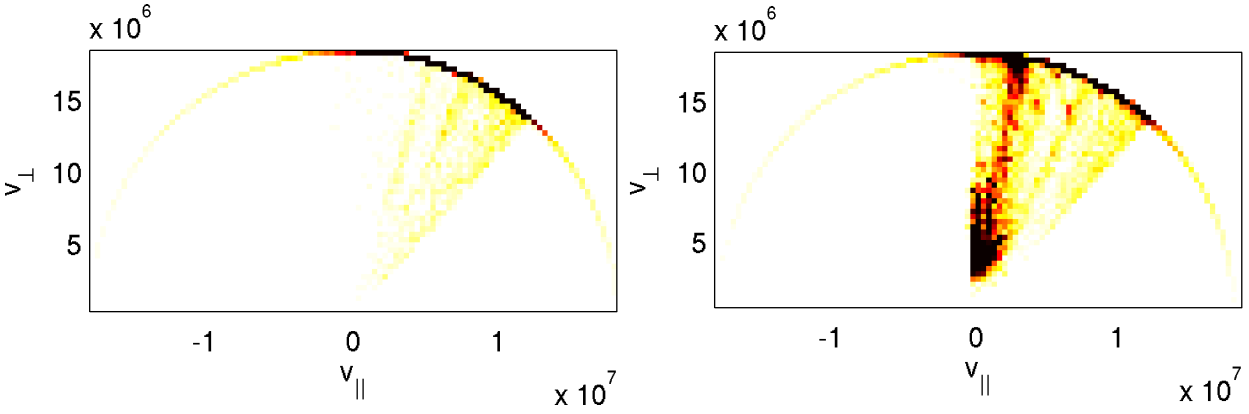

Figure 13: Comparison of losses in velocity-space between axisymmetric and 3D equilibrium (result is identical for 2D+ripple).

Figure 12(b) is a similar histogram based on flight time, i.e. seconds after which an alpha particle crosses the LCFS. The large peak on the left is again due to prompt losses, for timescales of the order of a bounce/transit period, $\sim 10^{-5}$s. The curve drops significantly at around 0.1s in the axisymmetric case, quicker than a slowing-down time. At low energies, particles thermalise faster (move out of the alpha population) than they diffuse outwards. The opposite behaviour is observed in the presence of ripple as the loss rate is enhanced for longer flight-times. The combined effect of ripple and collisionality leads to a stronger redistribution of particles in phase-space than in the axisymmetric case. The fact that ripple transport is more efficient at low energies is a favourable result for the current design of DEMO, allowing good power confinement and a sink for cold particles.

Figure 13 shows the lost particle distribution function in velocity space. The semi-circle denotes prompt losses at $\frac{1}{2}m(v_{||}^2+v_{\perp}^2) = 3.5MeV$. Colours are most vivid near the boundary between co-passing and trapped. Most losses occur on the outer midplane (see figure 14), which is easier to reach on the lower portion of a co-passing particle return path than on the upper portion of a counter-passing return path. In the axisymmetric case, the yellow inverted triangle is caused by particles switching from a narrow passing orbit to a wider trapped orbit after a collision. In the presence of ripple, a darker region appears in the vicinity of $v_{||} \sim 0$. This corresponds to deeply trapped particles that sit at the edge of the plasma and are kicked around the ripple-wells via collisions. This effect is stronger as particle energy decreases and leads to the enhancement of transport with collisionality, as mentioned above.

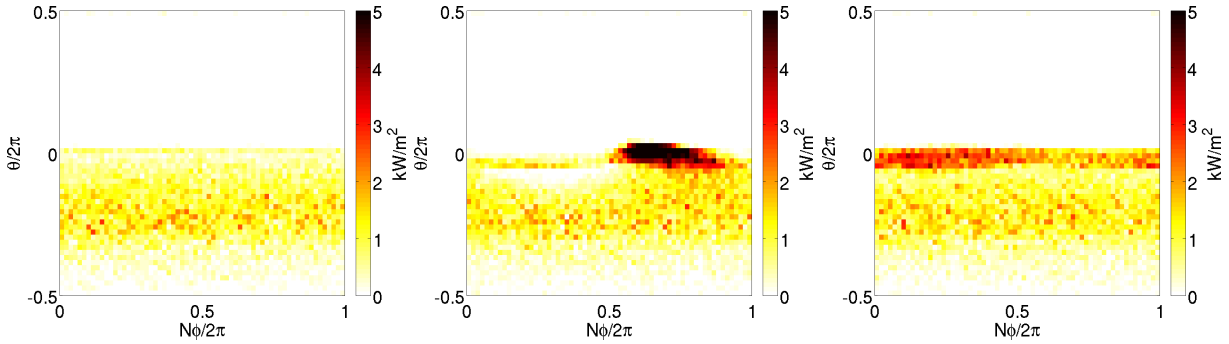

(a) Axisymmetric case (b) 2D+ripple model (c) 3D equilibrium model

Figure 14: Power flux through the LCFS as a function of toroidal and poloidal angles.

Figure 14 shows lost power fluxes through the LCFS as a function of the toroidal and the (VMEC) poloidal angle θ. Losses in the axisymmetric case are heavenly distributed in the toroidal direction and around $\theta \sim 0$ (outer midplane). In the 2D+ripple model, the simulation domain is the same axisymmetric LCFS but in this case, the field-lines, now three-dimensional, intersects the boundary. Particles streaming down the field-lines accumulate right after the location of the TF coil near $N\phi \sim 3\pi/2$, reminding that the magnetic field turns clockwise from above (opposite from the definition of toroidal angle). This hot spot is the result of a zero-orbit width effect, due to the intersection of field-lines with the boundary. In the 3D equilibrium case, the LCFS forms bulges consistently with the path of field-lines, such that particles are lost further away from the TF coil. These losses are due to drift effects. Their accumulation occurs in the region of unfavourable curvature near $N\phi \sim \pi/2$. The mechanism is similar to that observed in stellarators [34]. Ultimately, particles would continue to be followed in the vacuum beyond the LCFS. The matching of 3D equilibria and vacuum fields is difficult with present day tools such that it is currently not possible to compare heat loads in both ripple 2D+ripple and 3D equilibrium models. The difference between figure 14(b) and 14(c) is not however expected to translate to corresponding local hot-spots on the wall or plasma facing components, since the wall is many orbit widths away from the plasma, and deformations in the wall will be much larger than the differences in the magnetic between the two models. The calculation of exact heat-loads of plasma-facing components (PFCs) is addressed in the vacuum approximation by several other groups [35]. The formation of hot-spots mostly occur wherever the wall is protruding the vacuum vessel or the field-lines are intersecting the PFCs.

V. CONCLUSIONS

Alpha particle losses and consequential heat fluxes on the surface marking the plasma boundary have been calculated in 3D MHD equilibria that model the DEMO coil configuration. The work is primarily a physics study that compares the losses associated with two models that account for the breaking of axisymmetry due to the finite number of toroidal field coils. In contrast to studies into the effects of resonant magnetic perturbations on fast ion losses, it is found that the plasma response to the ripple associated with the finite number of toroidal field coils is weak, thus ensuring that the plasma response can be neglected.

The two approaches for including the ripple field have been applied to DEMO for a given coil description (notably with 18 toroidal field coils assuming no ferritic inserts) and for a given plasma current density and plasma pressure profile. For the study of particle trajectories, it was found that the guiding centre approximation is adequate, essentially because the scale length of the magnetic field variation is much larger that the Larmor radius of 3.5MeV alpha particles. A detailed investigation into the origin of the transport due to the 3D nature of the DEMO magnetic field was undertaken. It is found that the dominant transport channel is due to superbanana transport, enhanced by collisions. The relatively weak ripple does not cause magnetic islands to form, nor stochastic fields in the 2D+ripple model (note that islands are not permitted in the 3D equilibrium model), so that losses from passing ions are negligible. The approximate criterion for the onset of trapped ion stochastisation was reviewed for the use of general flux-coordinates (`VMEC`) and the regions of chaotic bounce tips were qualitatively mapped. Chaotic trapped ion stochastisation due to drift-bounce resonance is subdominant, although its contribution to transport is hard to predict and to disentangle within the full-F VENUS-LEVIS simulations.

By undertaking full-F slowing-down simulations for the distribution function of the alpha particles, using the guiding-centre code VENUS-LEVIS, it is found that the choice of model for the 3D ripple does affect the local power flux (locally in toroidal and poloidal angle) on the last closed flux surface, but not the total power given to the edge. The alpha population is well confined in the core of the plasma. The effect of the 3D magnetic field influences transport only near the edge of the plasma. The weak amount of alpha particle losses obtained in axisymmetry is increased by 50% due to ripple, with peak effect occurring for particles in the 100-200keV range. This convenient transport process for helium ash is

dominated by collisional super banana transport, rather than stochastic ripple transport.

Acknowledgments

The authors are indebted to the DEMO Basic Physics Group led by R. Wenninger at IPP/Garching for providing the coils and background plasma profiles. We also thank S. P. Hirshman for the use of the `VMEC` code for the equilibrium construction.

This work, supported by the Swiss National Science Foundation, has been carried out within the framework of the EUROfusion Consortium and has received funding from the Euratom research and training programme 2014-2018 under grant agreement No 633053. The views and opinions expressed herein do not necessarily reflect those of the European Commission. Simulations were performed on BlueGene cluster at EPFL, Lausanne (CH), on DORA cluster at CSCS, Manno (CH) and on Helios at CSC, Rokkasho (Japan).

---

[1] L. Eriksson and F. Porcelli, *Plasma Physics and Controlled Fusion* **43**, R145 (2001).

[2] R. Budny, M. Bell, H. Biglari, M. Bitter, C. Bush, C. Cheng, E. Fredrickson, B. Grek, K. Hill, H. Hsuan, A. Janos, D. Jassby, D. Johnson, L. Johnson, B. LeBlanc, D. McCune, D. Mikkelsen, H. Park, A. Ramsey, S. Sabbagh, S. Scott, J. Schivell, J. Strachan, B. Stratton, E. Synakowski, G. Taylor, M. Zarnstorff, and S. Zweben, *Nuclear Fusion* **32**, 429 (1992).

[3] M. Garcia-Munoz, S. Äkäslompolo, O. Asunta, J. Boom, X. Chen, I. Classen, R. Dux, T. Evans, S. Fietz, R. Fisher, C. Fuchs, B. Geiger, M. Hoelzl, V. Igochine, Y. Jeon, J. Kim, J. Kim, B. Kurzan, N. Lazanyi, T. Lunt, R. McDermott, M. Nocente, D. Pace, T. Rhodes, M. Rodriguez-Ramos, K. Shinohara, W. Suttrop, M. V. Zeeland, E. Viezzer, M. Willensdorfer, E. Wolfrum, the ASDEX Upgrade, DIII-D, and K. Teams, *Nuclear Fusion* **53**, 123008 (2013).

[4] M. A. V. Zeeland, N. M. Ferraro, W. W. Heidbrink, G. J. Kramer, D. C. Pace, X. Chen, T. E. Evans, R. K. Fisher, M. Garcia-Munoz, J. M. Hanson, M. J. Lanctot, L. L. Lao, R. A. Moyer, R. Nazikian, and D. M. Orlov, *Plasma Physics and Controlled Fusion* **56**, 015009 (2014).

[5] T. Kurki-Suonio, O. Asunta, T. Hellsten, V. Hynönen, T. Johnson, T. Koskela, J. Lönnroth, V. Parail, M. Roccella, G. Saibene, A. Salmi, and S. Sipilä, *Nuclear Fusion* **49**, 095001 (2009).

[6] N. Oyama, H. Urano, K. Shinohara, M. Honda, T. Takizuka, N. Hayashi, Y. Kamada, and the JT-60 Team, *Nuclear Fusion* **52**, 114013 (2012).

[7] P. N. Yushmanov, *Rev. Plasma Phys.* **16**, 117 (1990).

[8] K. G. McClements, *Physics of Plasmas* **12**, (2005).

[9] K. Shinohara, K. Tani, T. Oikawa, S. Putvinski, M. Schaffer, and A. Loarte, *Nuclear Fusion* **52**, 094008 (2012).

[10] K. Tani, M. Azumi, H. Kishimoto, and S. Tamura, *Journal of the Physical Society of Japan* **50**, 1726 (1981).

[11] R. J. Goldston, R. B. White, and A. H. Boozer, *Phys. Rev. Lett.* **47**, 647 (1981).

[12] J. R. Cary and S. G. Shasharina, *Physics of Fluids B* **5**, 2098 (1993).

[13] V. Marchenko, *Nuclear Fusion* **35**, 69 (1995).

[14] L. Eriksson and P. Helander, *Nuclear Fusion* **33**, 767 (1993).

[15] R. B. White, R. J. Goldston, M. H. Redi, and R. V. Budny, *Physics of Plasmas* **3**, 3043 (1996).

[16] P. Yushmanov, *Nuclear Fusion* **23**, 1599 (1983).

[17] H. Mynick, *Nuclear Fusion* **26**, 491 (1986).

[18] R. B. White and H. E. Mynick, *Physics of Fluids B* **1**, 980 (1989).

[19] D. Pfefferlé, C. Misev, W. A. Cooper, and J. P. Graves, *Nuclear Fusion* **55**, 012001 (2015).

[20] D. A. Spong, *Physics of Plasmas (1994-present)* **18**, (2011).

[21] W. A. Cooper, S. F. i Margalet, S. J. Allfrey, J. Kisslinger, H. F. G. Wobig, Y. Narushima, S. Okamura, C. Suzuki, K. Y. Watanabe, K. Yamazaki, and M. Y. Isaev, *Fusion Science and Technology* **46**, 365 (2004).

[22] S. Hirshman, W. van RIJ, and P. Merkel, *Computer Physics Communications* **43**, 143 (1986).

[23] D. Pfefferlé, W. Cooper, J. Graves, and C. Misev, *Computer Physics Communications* **185**, 3127 (2014).

[24] K. Miyamoto, *Plasma Physics for Nuclear Fusion*, The MIT Press, 1989.

[25] J. Rome, *Nuclear Fusion* **35**, 195 (1995).

[26] I. Chapman, D. Brunetti, P. Buratti, W. Cooper, J. Graves, J. Harrison, J. Holgate, S. Jardin, S. Sabbagh, K. Tritz, the MAST, N. Teams, and E.-J. Contributors, *Nuclear Fusion* **54**, 083007 (2014).

[27] S. Äkäslompolo, O. Asunta, T. Bergmans, M. Gagliardi, J. Galabert, E. Hirvijoki, T. Kurki-Suonio, S. Sipilä, A. Snicker, and K. Särkimäki, *Fusion Engineering and Design* **98–99**, 1039 (2015), Proceedings of the 28th Symposium On Fusion Technology (SOFT-28).

[28] J. B. Taylor, *Phys. Rev. Lett.* **33**, 1139 (1974).

[29] R. White, *The Theory of Toroidally Confined Plasmas*, Imperial College Press, 2014.

[30] Y. Kolesnichenko and V. Yavorskij, *Nuclear Fusion* **29**, 1319 (1989).

[31] R. G. Littlejohn, *Journal of Plasma Physics* **29**, 111 (1983).

[32] A. H. Boozer and G. Kuo-Petravic, *Physics of Fluids (1958-1988)* **24**, 851 (1981).

[33] H.-S. Bosch and G. Hale, *Nuclear Fusion* **32**, 611 (1992).

[34] F. Faustin, W. Cooper, J. Graves, D.Pfefferlé, and J.Geiger, *Nuclear Fusion* **submitted** (2016).

[35] E. Hirvijoki, A. Snicker, T. Korpilo, P. Lauber, E. Poli, M. Schneller, and T. Kurki-Suonio, *Computer Physics Communications* **183**, 2589 (2012).